



## Analysis and design of pulse frequency modulation dielectric barrier discharge for low power applications\*

Tang-tang GUO<sup>†</sup>, Xing-liang LIU, Shi-qiang HAO, Chi ZHANG, Xiang-ning HE<sup>†‡</sup>

(School of Electrical Engineering, Zhejiang University, Hangzhou 310027, China)

<sup>†</sup>E-mail: gtt1024@gmail.com; hxn@zju.edu.cn

Received May 16, 2014; Revision accepted Aug. 8, 2014; Crosschecked Jan. 28, 2015

**Abstract:** For low power dielectric barrier discharge (DBD) used in small-size material treatment or portable devices, high-step transformer parasitic capacitance greatly influences the performance of the resonant converter as it is of the same order of magnitude as the equivalent capacitance of DBD load. In this paper, steady-state analysis of the low power DBD is presented, considering the inevitable parasitic capacitance of the high-step transformer. The rectifier-compensated first harmonic approximation (RCFHA) is applied to linearize the equivalent load circuit of DBD at low frequency and the derived expressions are accurate and convenient for the analysis and design of the power supply. Based on the proposed linear equivalent load circuit, the influence of transformer parasitic capacitance on the key parameters, including the frequency range and the applied electrode voltage, is discussed when the power is regulated with pulse frequency modulation (PFM). Also, a design procedure is presented based on the derived expressions. A prototype is constructed according to the design results and the accuracy of the design is verified by experimental results.

**Key words:** Dielectric barrier discharge, Rectifier-compensated first harmonic approximation, Parasitic capacitance, Power converter design

doi:10.1631/FITEE.1400185

Document code: A

CLC number: TM46

### 1 Introduction

Dielectric barrier discharge (DBD) has been widely used in material treatment, ozone generation, biomedicine, etc. The plasma or ozone generated during discharge can be used for material surface characteristic modification, sterilization, and chemical vapor deposition (Fang *et al.*, 2006; Wang and He, 2006; Burany *et al.*, 2008; Wedaa *et al.*, 2011; Kostov *et al.*, 2013).

Usually, an AC high voltage is applied to the load as shown in Fig. 1a to generate discharge for industrial applications due to easy power regulation

methods, simple topology, and high reliability. When the applied voltage is high enough, the air between the dielectric and the high voltage electrode breaks down and a corona discharge is initiated. As the voltage across the air gap is almost constant when a corona discharge occurs (Alonso *et al.*, 2003), the equivalent circuit of the DBD load is as illustrated in Fig. 1a, where  $C_{g_s}$  represents the equivalent capacitance of the air gap, and  $C_{d_s}$  represents the equivalent capacitance of the dielectric (Wagner *et al.*, 2003; Williamson *et al.*, 2006; Bonaldo and Pomilio, 2010). The diode bridge circuit models the bidirectional voltage clamping properties of the constant corona discharge voltage. To produce the required AC high voltage, the resonant converter is usually applied, as well as a high-frequency high-step transformer which leads to galvanic isolation.

In high power DBD applications, the parasitic capacitance of the transformer is much smaller than

<sup>‡</sup> Corresponding author

\* Project supported by the National Natural Science Foundation of China (No. 51107115) and the China Postdoctoral Science Foundation (No. 20110491766)

ORCID: Tang-tang GUO, <http://orcid.org/0000-0002-9603-0997>  
 © Zhejiang University and Springer-Verlag Berlin Heidelberg 2015

the equivalent capacitance of DBD load and thus negligible. Therefore, an inductor-capacitor-capacitor (LCC) series-parallel resonant converter is used as the equivalent circuit, which has been discussed in many papers (Gilbert *et al.*, 2007; Fu *et al.*, 2008; Martin-Ramos *et al.*, 2008). However, in low power applications, such as small-size material treatment or the portable medical device, the equivalent capacitance of DBD load and the transformer parasitic capacitance are of the same order of magnitude. Thus, parasitic capacitance must be taken into consideration and the conventional LCC resonant converter is no more suitable for analysis. The influence of parasitic capacitance should be discussed. Moreover, for higher portability and lower cost, the resonant inductor is integrated into the transformer by applying a magnetic integration technique (Fu *et al.*, 2008). Therefore, only one magnetic component is required (Fig. 1b).

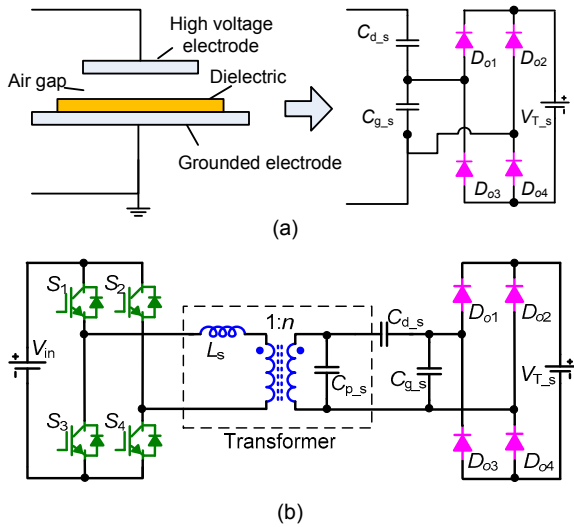


**Fig. 1** Equivalent circuits of DBD load (a) and the whole resonant converter (b)

The notations used in this paper are given in Table 1.

To simplify the analysis, a capacitance in parallel with a resistance (RC) is used as the equivalent circuit of DBD load based on first harmonic approximation (FHA) (Alonso *et al.*, 2003; Kinnares and Hothongkham, 2010). However, FHA is not accurate enough for steady-state analysis due to the diode bridge circuit. Therefore, rectifier-compensated first harmonic approximation (RCFHA) (Shafiei *et al.*,

**Table 1** The notations used in this paper

Parameter	Meaning
$C_d$	Dielectric equivalent capacitance referred to the primary side of the transformer
$C_g$	Air gap equivalent capacitance referred to the primary side of the transformer
$V_T$	Discharge maintaining voltage referred to the primary side of the transformer
$L_s$	Leakage inductance of the transformer
$C_p$	Transformer parasitic capacitance referred to the primary side of the transformer
$n$	Transformer turns ratio
$f_s$	Operating frequency
$\omega_s$	Operating angular frequency, $\omega_s=2\pi f_s$
$f_0$	Resonant frequency
$V_{in}$	Bus voltage applied to the inverter
$v_{ab}$	Output voltage of the inverter
$v_{ae}$	Voltage applied to electrodes
$V_{ae}$	Peak value of $v_{ae}$
$G_r$	Resonant tank gain, $G_r=V_{ae}/(nV_{in})$
$v_{cd}$	Voltage applied to $C_d$
$i_{cd}$	Current flowing through $C_d$
$v_{cg}$	Voltage applied to $C_g$
$i_r$	Resonant current referred to the primary side of the transformer
$I_r$	Peak value of $i_r$
$P_{in}$	Average input power
$P_{out}$	Average output power
$k_s$	Load equivalent capacitance ratio, $k_s=C_d/C_g$
$k_p$	$k_p=C_p/C_d$
$\psi$	The angle of charging $C_g$
$\varphi$	Phase error between the output voltage of the inverter and resonant current
$t_{db}$	Dead band time
$t_d$	Time delay between the rising edge of driving signals and the corresponding zero-crossing point of the resonant current
$t_{pe}$	Time delay between the rising edge of the full-bridge output voltage and the resonant current
$X_{y\_norm}$	Normalized variable $X_y$
$X_{y\_s}$	Variable $X_y$ , referred to the secondary side of the transformer
$X_{y1}$	Fundamental harmonic component of $X_y$
$X_{yA}$	Coefficient of the Fourier sinusoidal term of $X_{y1}$ at $f_s$
$X_{yB}$	Coefficient of the Fourier cosinusoidal term of $X_{y1}$ at $f_s$

2013) is used for the steady-state analysis of the resonant converter with a rectified bridge. According to the equivalent circuit derived, the impact of

transformer parasitic capacitance on the frequency range and applied electrode voltage is discussed when the power is regulated with pulse frequency modulation (PFM), considering the different equivalent load parameters with varied output power (Wang et al., 2005). Then the design procedure is presented with the magnetic integration technique and the leakage inductance and parasitic capacitance of the transformer are given according to the results of steady-state analysis. The analysis and design are finally verified by simulation and experimental results.

## 2 Converter analysis

### 2.1 Steady-state analysis

A capacitor in series with a resistor is used to model  $C_g$  and the rectifier in RCFHA. Thus, the analysis is more accurate than that in FHA, where a resistor is used for equivalence. To simplify the analysis, all the parameters are referred to the primary side of the transformer (Fig. 2a).

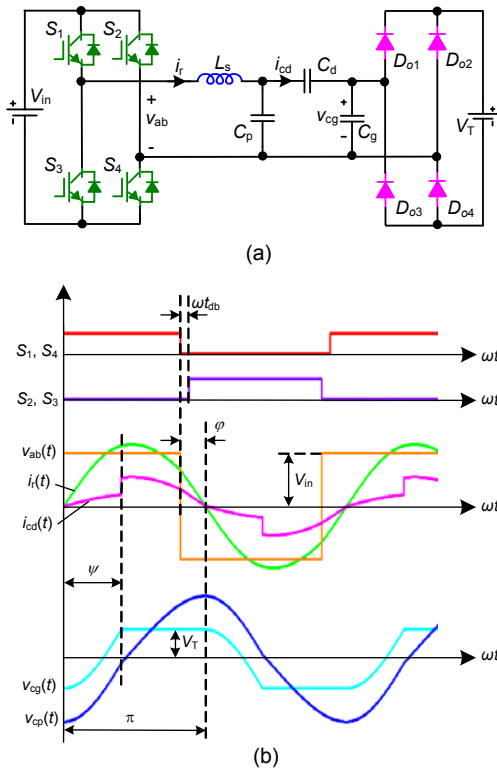


Fig. 2 Equivalent circuit of low power DBD referred to the primary side (a) and the key waveforms (b)

The key waveforms of the resonant converter are shown in Fig. 2b. As  $i_r(t)$  is almost sinusoidal, it is assumed to be equal to its first harmonic component. That is,

$$i_{r1}(t) = i_r(t) = I_r \sin(\omega_s t). \quad (1)$$

According to whether  $C_g$  is clamped or not, the circuit operation can be divided into four stages. In the first half cycle, when  $i_r(t)$  increases from zero,  $C_g$  is charged from  $-V_T$  and the equivalent circuit is as shown in Fig. 3a. Thus, the following equations can be obtained:

$$i_{cd}(t) = \frac{1}{1+k_p+k_p k_s} I_r \sin(\omega_s t), \quad (2)$$

$$v_{cg}(t) = -V_T + \frac{I_r}{\omega_s C_g (1+k_p+k_p k_s)} (1 - \cos(\omega_s t)). \quad (3)$$

At the end of this stage,  $v_{cg}(t)$  increases to  $V_T$ . That is,

$$v_{cg} \left( \frac{\psi}{\omega_s} \right) = V_T. \quad (4)$$

By substituting Eq. (4) into Eq. (3), the following equation can be derived:

$$\cos \psi = 1 - \frac{2V_T \omega_s C_g (1+k_p+k_p k_s)}{I_r}. \quad (5)$$

Then  $C_g$  is charging to  $V_T$  and is clamped until  $i_r(t)$  oscillates to zero. Thus, the equivalent circuit turns into the circuit shown in Fig. 3b. During this stage,  $i_{cd}(t)$  and  $v_{cg}(t)$  are given by

$$i_{cd}(t) = \frac{1}{1+k_p} I_r \sin(\omega_s t), \quad (6)$$

$$v_{cg}(t) = V_T. \quad (7)$$

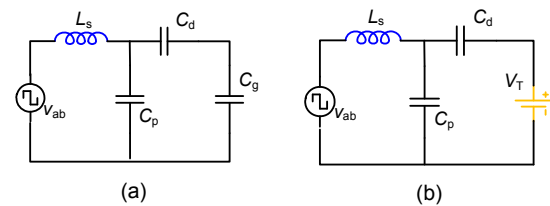


Fig. 3 Equivalent circuits when  $C_g$  is charging (a) and clamped (b)

The power transfers to the load during this stage. So, the output power can be obtained by integrating  $v_{cg}(t)$  and  $i_{cd}(t)$ :

$$P_{out} = \frac{V_T I_r (1 + \cos \psi)}{\pi} \frac{1}{1 + k_p} \quad (8)$$

Due to symmetry,  $i_{cd}(t)$  and  $v_{cg}(t)$  in one period can be summarized to be

$$i_{cd}(t) = \begin{cases} \frac{1}{1 + k_p + k_p k_s} I_r \sin(\omega_s t), & 0 \leq t < \frac{\psi}{\omega_s} \text{ or } \pi \leq t < \frac{\pi + \psi}{\omega_s}, \\ \frac{1}{1 + k_p} I_r \sin(\omega_s t), & \frac{\psi}{\omega_s} \leq t < \pi \text{ or } \frac{\pi + \psi}{\omega_s} \leq t < 2\pi, \end{cases} \quad (9)$$

$$v_{cg}(t) = \begin{cases} -V_T + \frac{I_r}{\omega_s C_g (1 + k_p + k_p k_s)} (1 - \cos(\omega_s t)), & 0 \leq t < \psi / \omega_s, \\ V_T, & \psi / \omega_s \leq t < \pi, \\ V_T - \frac{I_r}{\omega_s C_g (1 + k_p + k_p k_s)} (1 + \cos(\omega_s t)), & \pi \leq t < \frac{\pi + \psi}{\omega_s}, \\ -V_T, & \frac{\pi + \psi}{\omega_s} \leq t < 2\pi. \end{cases} \quad (10)$$

Using the Fourier analysis, the coefficients of the Fourier series of  $i_{cd}(t)$  and  $v_{cg}(t)$  are obtained as

$$I_{cdA} = \frac{I_r}{2\pi(1 + k_p)(1 + k_p + k_p k_s)} \cdot [(\sin(2\psi) + 2\pi - 2\psi)k_p k_s + 2\pi(1 + k_p)], \quad (11)$$

$$I_{cdB} = \frac{-I_r k_p k_s \sin^2 \psi}{\pi(1 + k_p)(1 + k_p + k_p k_s)}, \quad (12)$$

$$V_{cgA} = \frac{I_r \sin^2 \psi}{\pi C_g \omega_s (1 + k_p + k_p k_s)}, \quad (13)$$

$$V_{cgB} = \frac{-I_r}{2\pi C_g \omega_s (1 + k_p + k_p k_s)} (2\psi - \sin(2\psi)). \quad (14)$$

Thus, the equivalent impedance can be derived:

$$Z_{eq} = \frac{V_{cgA} + jV_{cgB}}{I_{cdA} + jI_{cdB}} = R_{eq} + jX_{eq}, \quad (15)$$

where  $R_{eq}$  and  $X_{eq}$  are given in Eqs. (16) and (17), respectively:

$$R_{eq} = \pi(1 + k_p)(1 + k_p + k_p k_s) \sin^2 \psi \cdot \{C_g \omega_s \{(k_p k_s \sin^2 \psi)^2 + [\pi(1 + k_p + k_p k_s) - k_p k_s (\psi - \sin \psi \cos \psi)]^2\}\}^{-1}, \quad (16)$$

$$X_{eq} = -(1 + k_p) \{ \pi(1 + k_p + k_p k_s) (\psi - \sin \psi \cos \psi) - [(\psi - \sin \psi \cos \psi)^2 + \sin^4 \psi] k_p k_s \} \cdot \{C_g \omega_s \{(k_p k_s \sin^2 \psi)^2 + [\pi(1 + k_p + k_p k_s) - k_p k_s (\psi - \sin \psi \cos \psi)]^2\}\}^{-1}, \quad (17)$$

Consequently, the equivalent circuit of RCFHA is obtained (Fig. 4a), where  $C_{eq} = -1/(\omega_s X_{eq})$ . By combining  $C_d$  and  $C_{eq}$ , the circuit can be simplified further (Fig. 4b), where  $C_e = C_d C_{eq} / (C_d + C_{eq})$ . Thus, the resonant converter shown in Fig. 1b is greatly simplified and the input impedance is derived as follows:

$$Z_{in} = R_{in} + jX_{in}, \quad (18)$$

where

$$R_{in} = \frac{R_{eq} C_e^2}{(C_p + C_e)^2 + (\omega_s C_e C_p R_{eq})^2}, \quad (19)$$

$$X_{in} = \omega_s L_s - \frac{C_p + C_e + C_p \omega_s^2 C_e^2 R_{eq}^2}{\omega_s (C_p + C_e)^2 + \omega_s^3 C_p^2 C_e^2 R_{eq}^2}. \quad (20)$$

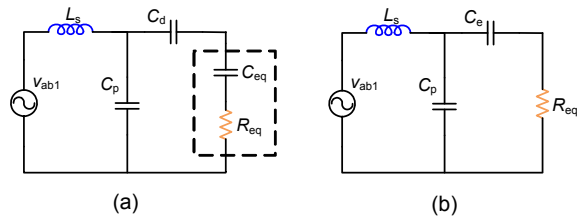


Fig. 4 Equivalent circuit of Fig. 2a in a steady condition (a) and the simplified circuit (b)

The phase error between the output voltage of the inverter and the resonant current, the peak resonant current and the peak applied electrode voltage are given in Eqs. (21)–(23), corresponding to the

equivalent circuit in Fig. 4b:

$$\tan \varphi = X_{in} / R_{in}, \quad (21)$$

$$I_r = \frac{4V_{ab}}{\pi\sqrt{R_{in}^2 + X_{in}^2}}, \quad (22)$$

$$V_{ae} = I_r\sqrt{R_{in}^2 + X_{in}^2}. \quad (23)$$

The key parameters of the converter, including the peak applied electrode voltage, peak resonant current, resonant frequency, and quality factor, can be obtained from Eqs. (16)–(23). Therefore, the equivalent circuit shown in Fig. 4b can be used to describe the performance of low power DBD for simplicity.

## 2.2 Performance analysis

PFM is usually used to regulate the output power due to the simple control strategy and zero-voltage switch (ZVS) (Liu and He, 2005). The output power decreases with an increased operating frequency and ZVS is achieved for the whole power range. A narrow range of operating frequencies is preferred for the resonant converter from light load to full load, as the breakdown voltage of the transformer decreases significantly with increased frequency (Shafiei *et al.*, 2011).

On the other hand, the peak applied electrode voltage, which plays an important role in the number of microdischarges and surface treatment effect (Gibalov and Pietsch, 2000; Jidenko *et al.*, 2006), varies with the output power. In material treatment, the high applied electrode voltage may ruin or even burn the materials, while the low voltage may make the discharge unstable and result in uneven treatment. Consequently, it is necessary to investigate the influence of  $C_p$  on  $f_s$  and  $V_{ae}$ .

When the resonant tank operates at resonance, it is resistive and hence the resonant frequency can be derived from Eq. (20). Fig. 5 illustrates the operating frequency and tank gain at resonance with variant  $C_p$ . The resonant frequency increases with decreased  $C_p$ , which results in high power density. However, the tank gain of the resonant converter diminishes in the meantime and the voltage pressure of the switches increases when a constant  $V_{ae}$  is required for stable discharge. Hence, a tradeoff should be made if necessary.

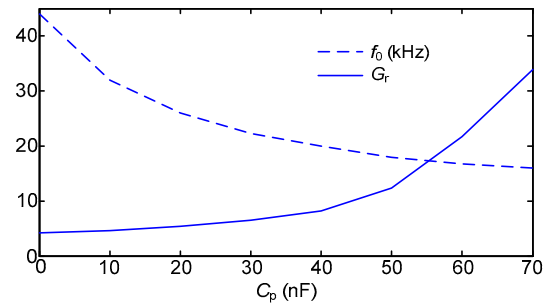


Fig. 5 Resonant frequency and tank gain with variant  $C_p$

To simplify the analysis in PFM, the normalized results are used (Gilbert *et al.*, 2007). The normalized frequencies of the resonant converter from full load to light load with variant  $C_p$  are as illustrated in Fig. 6a, where  $C_p=0$  represents that the converter is the conventional LCC resonant converter without parasitic capacitance. Fig. 6b shows the normalized peak applied electrode voltage. What is more, the equivalent capacitance of DBD load varies with the peak applied electrode voltage.  $C_d$  decreases from 48 nF to 32 nF with decreased  $V_{ae}$ , while  $C_g$  is assumed to be a constant of 16 nF, corresponding to the conclusions in Wang *et al.* (2005). The curves in Fig. 6a demonstrate that a larger  $C_p$  results in a narrower frequency range from full load to light load as  $C_p$  counteracts the influence of non-constant equivalent capacitance of DBD load, which simplifies the transformer design and improves the reliability. On the other hand,  $V_{ae}$  decreases faster in PFM with a larger  $C_p$ , which may influence the discharge stability and change the characteristics. Therefore, a compromise should be made when selecting  $C_p$  according to the requirements.

## 3 Design considerations

Based on the expressions derived in Section 2, the design procedure for a specified DBD load is presented as an example. The DBD load consists of two round planar electrodes and a 1 mm thick, flat piece of quartz as the dielectric as shown in Fig. 1a. The diameters of the high voltage electrode, quartz dielectric, and grounded electrode are 3, 5, and 6 cm, respectively. The parameters of the load in rated conditions are listed in Table 2. In a resonant converter with DBD load, the operating frequency is a

little higher than the resonant frequency for ZVS as shown in Fig. 7. When switches  $S_1$  and  $S_4$  are turned on, the resonant current flows through the reverse parallel diodes and the voltage through the two switches is zero. Thus, ZVS is achieved and  $t_d$  is defined to be the time delay between the rising edge of the driving signals and the corresponding zero-crossing point of the current. By adding the dead band,  $t_{db}$ , to  $t_d$ , the total time the output voltage of the inverter leading the resonant current,  $t_{pe}$ , is obtained. In this study,  $t_{db}$  and  $t_{pe}$  are specified to be 2  $\mu$ s and 4  $\mu$ s in the rated condition, respectively.

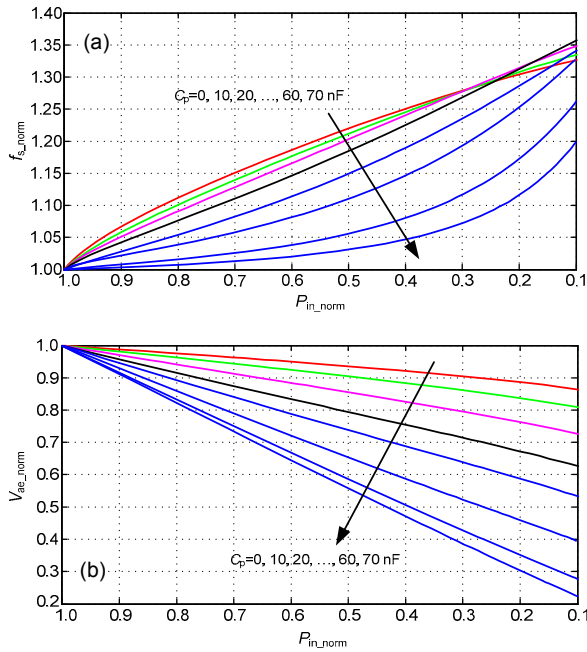


**Fig. 6 Performance comparison of variant  $C_p$  in the normalized frequency (a) and the normalized applied electrode voltage with PFM (b)**

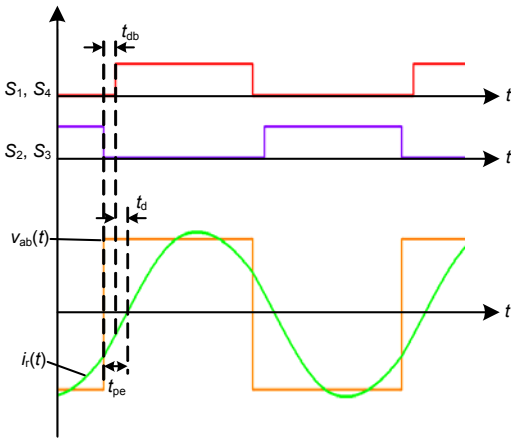


**Fig. 7 Zero-voltage switch (ZVS) waveforms**

**Table 2 Converter specification**

Parameter	Value
$P_{in}$	26 W
$C_d$	30 pF
$C_g$	10 pF
$V_T$	2900 V
$V_{ab}$	24 V
$f_s$	20 kHz
$t_{pe}$	4 $\mu$ s

As the magnetic integration technique is applied,  $n$ ,  $L_s$ , and  $C_p$  are the only three parameters required to be determined. For explicit  $n$  and  $C_p$ ,  $I_r$  and  $\psi$  can be deduced by combining Eqs. (5) and (8):

$$I_r = \frac{\pi P_{in}(1+k_p)}{2V_T} + V_T \omega_s C_g (1+k_p+k_p k_s), \quad (24)$$

$$\psi = \arccos \left( \frac{\pi P_{in}(1+k_p) - 2V_T^2 \omega_s C_g (1+k_p+k_p k_s)}{\pi P_{in}(1+k_p) + 2V_T^2 \omega_s C_g (1+k_p+k_p k_s)} \right). \quad (25)$$

Thus,  $R_{eq}$ ,  $X_{eq}$ , and  $R_{in}$  are obtained, corresponding to Eqs. (16), (17), and (19), respectively. Then  $L_s$  can be derived by substituting Eqs. (19), (20), and (24) into Eq. (22):

$$L_s = \sqrt{\left( \frac{4V_{ab}}{\pi \omega_s I_r} \right)^2 - \left( \frac{R_{in}}{\omega_s} \right)^2} + \frac{C_p + C_e + C_p \omega_s^2 C_e^2 R_{eq}^2}{\omega_s^2 (C_p + C_e)^2 + \omega_s^4 C_p^2 C_e^2 R_{eq}^2}. \quad (26)$$

$X_{in}$  is obtained by substituting Eq. (26) into Eq. (20). Then  $\phi$  is calculated according to Eq. (21). And

$$t_{pe} = \frac{\phi}{\omega_s}. \quad (27)$$

The 3D figure in Fig. 8a illustrates  $t_{pe}$  with variant  $n$  and  $C_p$  corresponding to Eq. (27) and the curves of  $L_s$  are given in Fig. 8b according to Eq. (26). The design procedure can be subdivided into the following steps based on the curves:

Step 1: Select  $n$  and  $C_p$ . The purple curve in Fig. 8a includes the points at which  $t_{pe}$  is 4  $\mu$ s. Here  $n$  is selected to be 40 for convenient calculation, a low transformer turns ratio and hence a small  $C_p$  for

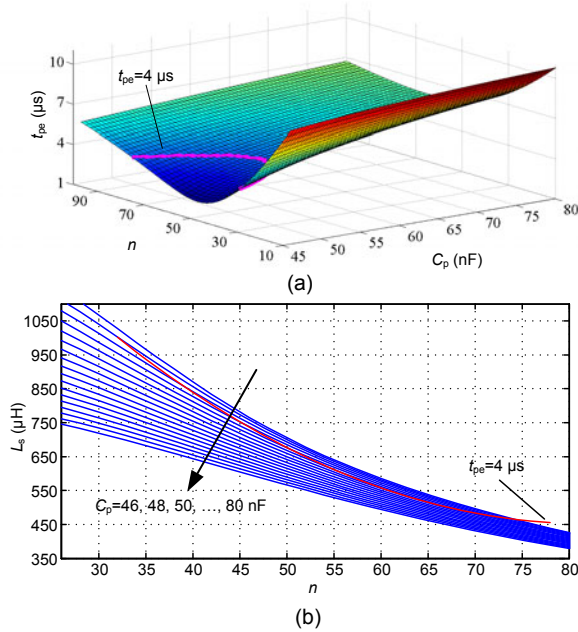


**Fig. 8** Design curves at variant  $C_p$  and  $n$ : (a)  $t_{pe}$ ; (b)  $L_s$ . References to color refer to the online version of this figure

the narrow applied electrode voltage range from full load to light load as presented in Section 2. Consequently,  $C_p$  is 52 nF.

Step 2: Calculate the transformer leakage inductance. The red curve in Fig. 8b represents the pairs of  $C_p$  and  $n$  at which  $t_{pe}$  is 4  $\mu$ s. Thus,  $L_s$  is determined to be 827  $\mu$ H corresponding to the parameters determined in Step 1.

Step 3: Calculate current stress. The peak resonant current is 1.94 A according to Eq. (24) for the specified  $n$  and  $C_p$ , which is helpful for selecting switches.

Step 4: Check the tolerance of  $C_p$  and  $L_s$ .  $C_p$  is highly affected by the structure of windings and the insulated materials used between the layers (Shafiei *et al.*, 2011). Moreover, in high voltage applications, a core type transformer is usually used for its high insulating property, and the leakage inductance is difficult to calculate (Doebbelin *et al.*, 2008). Thus,  $C_p$  and  $L_s$  cannot be designed exactly and the error tolerance should be taken into account. Table 3 lists the key parameters when  $C_p$  and  $L_s$  are changed by 10%. It shows that 10% errors of  $C_p$  and  $L_s$  bring approximately a 15% error in the rated power when  $t_{pe}$  is fixed to be 4  $\mu$ s. However, a tiny change of the operating frequency, no more than 9%, guarantees the required rated power and ZVS is still achieved.

Therefore, a minor error of  $C_p$  and  $L_s$  in the prototype is tolerable.

**Table 3** The key parameters when  $C_p$  and  $L_s$  are changed by 10%

Parameter	Value				
	$C_p=52$ nF, $L_s=827$ $\mu$ H	$C_p=47$ nF, $L_s=744$ $\mu$ H		$C_p=57$ nF, $L_s=910$ $\mu$ H	
		Fixed	Fixed	Fixed	Fixed
$t_{pe}$ ( $\mu$ s)		$t_{pe}$	$P_{in}$	$t_{pe}$	$P_{in}$
$P_{in}$ (W)	26.0	23.0	26.2	29.8	26.5
$I_r$ (A)	1.94	1.78	1.91	2.17	2.03
$f_s$ (kHz)	20.0	22.3	21.8	18.1	18.4
$t_{pe}$ ( $\mu$ s)	4.00	4.06	3.28	3.99	4.71

## 4 Simulation and experimental results

A prototype of the transformer shown in Fig. 9 is built corresponding to the parameters obtained in the design procedure, and the practical transformer parameters are listed in Table 4. The magnetic core comprises a pair of UF120A/70/30, which is Mn-Zn ferrite material.



**Fig. 9** Transformer prototype

**Table 4** Transformer parameters

Parameter	Value	
	Design	Prototype
$n$	40	40
$C_p$	52 nF	49 nF
$L_s$	827 $\mu$ H	880 $\mu$ H

A low power DBD system with the built transformer is used to verify the equivalent circuit and design procedure. In practice,  $C_p$  is 54 nF in the calculation as the high voltage probe (P6015, Tektronix) results in an extra 3 pF capacitance referred to the

secondary side (approximate 5 nF referred to the primary side of the transformer) in parallel with the load when measuring the applied electrode voltage. Fig. 10a illustrates the simulation waveforms corresponding to the prototype parameters while neglecting the parasitic capacitance, which differs greatly from the experimental waveforms in Fig. 10d. Consequently,  $C_p$  greatly influences the performance of DBD and should be carefully taken into consideration. In comparison with the experimental waveforms, the simulation waveforms from the converter with a rectified bridge as shown in Fig. 1b and the converter with an equivalent resonant model as shown in Fig. 4b are illustrated in Figs. 10b and 10c, respectively. There is a voltage drop when the current commutes from the diodes to the switches due to the switches' turn-on voltage and the diodes' forward voltage drop. Table 5 lists the key parameters of simulation, calculation with an equivalent model, and experiments, which confirm the steady-state analysis and design procedure a good accuracy.

The output power is regulated by PFM and  $t_{pe}$  is the control variable with self-sustained oscillation to maintain ZVS (Youssef and Jain, 2007; Gilbert et al.,

**Table 5 Simulation, calculation, and experimental results in rated conditions**

Parameter	Value		
	Simulation with $C_p$	Calculation	Experiments
$P_{in}$ (W)	26.6	27.3	26.8
$I_r$ (A)	1.91	1.98	2.05
$f_s$ (kHz)	19.0	19.0	18.1
$t_{pe}$ ( $\mu$ s)	4.03	3.91	4.00
$V_{ae}$ (kV)	7.86	8.03	7.76

2008). Figs. 11a–11c show the experimental waveforms at variant frequencies, which illustrate that the input power of the resonant tank decreases with the increased frequency and that ZVS is achieved in the whole power range. When  $t_{pe}$  is larger than 10  $\mu$ s, the applied electrode voltage is too low and the discharge in the air gap almost disappears. Table 6 gives the key parameters of the converter with an equivalent model, in comparison with the experimental results at variant frequencies, which verifies the accuracy of the equivalent resonant tank in steady-state conditions at different power levels.

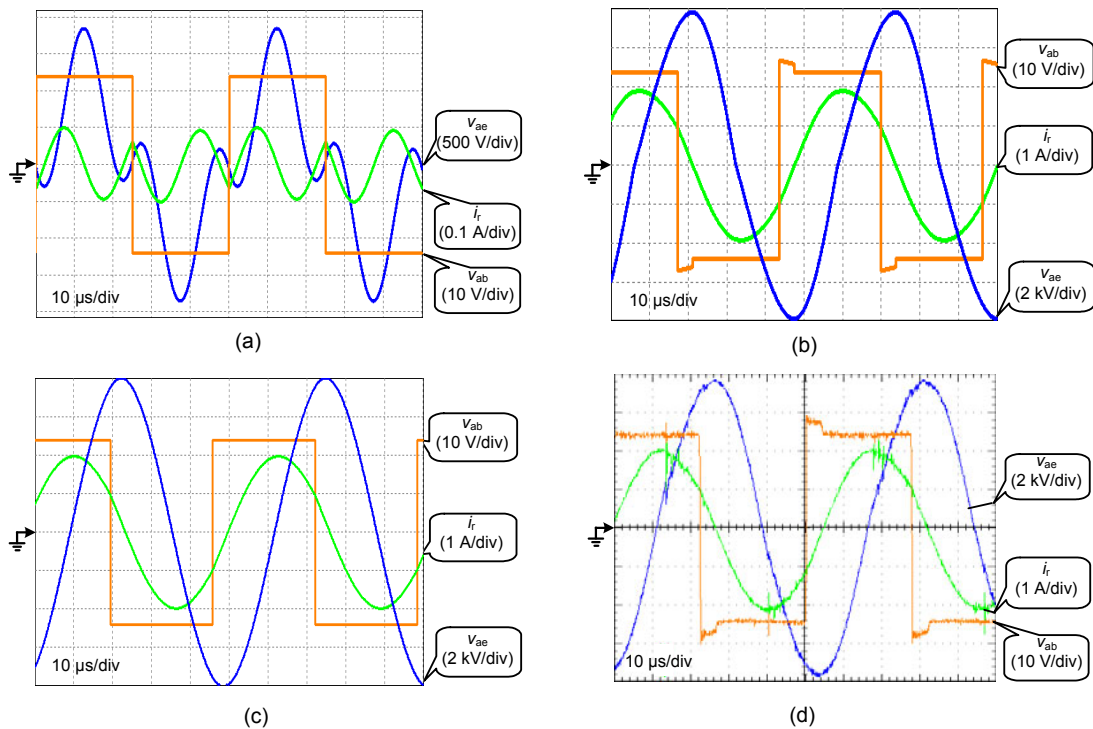


**Fig. 10 Waveforms of  $i_r$ ,  $v_{ab}$ , and  $v_{ae}$  in a rated condition in simulation without  $C_p$  (a), simulation from Fig. 1b (b), simulation with an equivalent model from Fig. 4b (c), and experiments (d)**

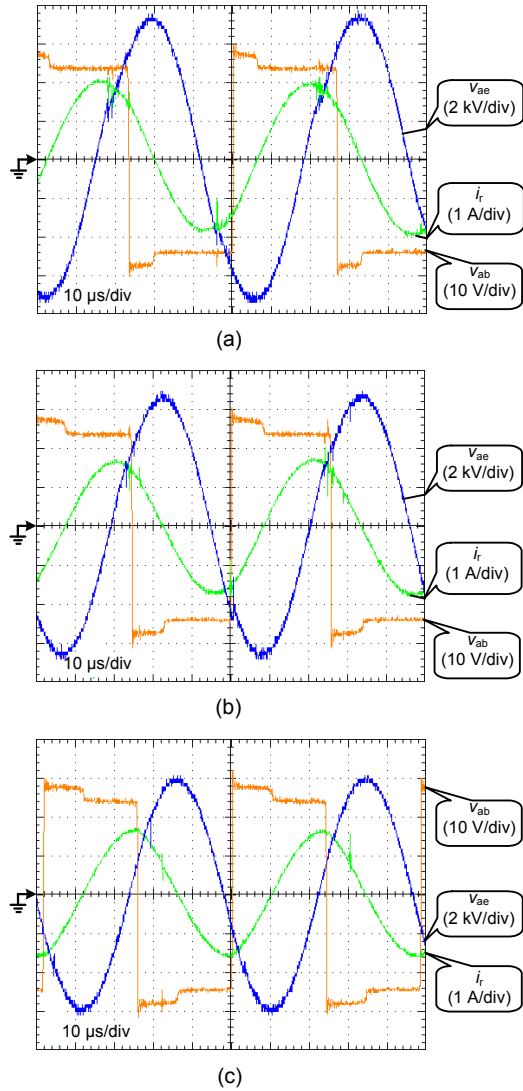


Fig. 11 Experimental waveforms when  $t_{pe}=6 \mu s$  (a),  $t_{pe}=8 \mu s$  (b), and  $t_{pe}=10 \mu s$  (c)

Table 6 Calculation and experimental results at variant frequencies

$t_{pe}$ ( $\mu s$ )	$P_{in}$ (W)		$f_s$ (kHz)		$I_r$ (A)		$V_{ae}$ (kV)	
	Cal.	Exp.	Cal.	Exp.	Cal.	Exp.	Cal.	Exp.
6	23.3	23.0	19.6	18.7	1.92	1.95	7.75	7.80
8	15.4	15.3	20.7	19.6	1.81	1.75	7.36	6.80
10	4.59	4.53	21.8	20.7	1.57	1.65	6.17	6.00

Cal.: calculation result; Exp.: experimental result

As RCFHA is based on the sinusoidal resonant current, the accuracy of the equivalent model is greatly influenced by the total harmonic distortion (THD) of the resonant current. Fig. 12 illustrates the

harmonic magnitude of the experimental resonant current as a percentage of the fundamental amplitude in the rated condition. Table 7 gives the THDs of the resonant current at variant frequencies derived from the simulation and experimental waveforms, which confirm that RCFHA is accurate in all steady-state conditions when power is regulated by the operating frequency. Therefore, the equivalent model is able to replace the original resonant converter with a rectified bridge for simpler performance analysis and design procedure.

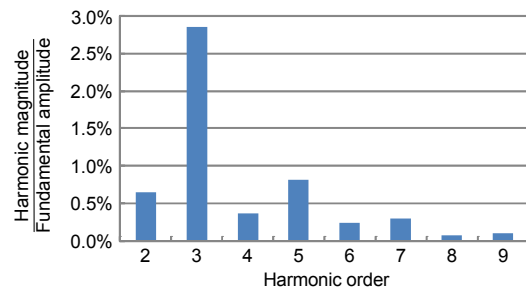


Fig. 12 Harmonic magnitude of experimental resonant current as a percentage of the fundamental amplitude in the rated condition

Table 7 The total harmonic distortion (THD) of resonant current at variant frequencies

$f_s$ (kHz)	THD	
	Simulation	Experiment
18.1	3.16%	3.10%
18.7	2.29%	2.69%
19.6	1.40%	2.16%
20.7	2.62%	2.89%

## 5 Conclusions

The power supply with a high-step transformer for low power DBD was investigated, taking the parasitic capacitance of the transformer into consideration. RCFHA was used in steady-state analysis and the derivation was given in detail, corresponding to the equivalent circuit of DBD load. The parasitic capacitance greatly influences the converter performance in low power DBD applications and a compromise between the small frequency difference and the stable peak electrode voltage should be made when determining its value. The design procedure of

the power supply was presented with the magnetic integration technique according to the expressions derived by an example. Finally, a prototype with two planar electrodes was built according to the design parameters and the experimental results were in good agreement with the design.

## References

- Alonso, J.M., Valdés, M., Calleja, A.J., et al., 2003. High frequency testing and modeling of silent discharge ozone generators. *Ozone Sci. Eng.*, **25**(5):363-376. [doi:10.1080/01919510390481685]
- Bonaldo, J.P., Pomilio, J.A., 2010. Control strategies for high frequency voltage source converter for ozone generation. Proc. IEEE Int. Symp. on Industrial Electronics, p.754-760. [doi:10.1109/ISIE.2010.5637402]
- Burany, N., Huber, L., Pejovic, P., 2008. Corona discharge surface treater without high voltage transformer. *IEEE Trans. Power Electron.*, **23**(2):993-1002. [doi:10.1109/TPEL.2007.915760]
- Doebbelin, R., Benecke, M., Lindemann, A., 2008. Calculation of leakage inductance of core-type transformers for power electronic circuits. Proc. 13th Power Electronics and Motion Control Conf., p.1280-1286. [doi:10.1109/EPEPEMC.2008.4635445]
- Fang, Z., Qiu, X., Qiu, Y., et al., 2006. Dielectric barrier discharge in atmospheric air for glass-surface treatment to enhance hydrophobicity. *IEEE Trans. Plasma Sci.*, **34**(4):1216-1222. [doi:10.1109/TPS.2006.877619]
- Fu, D., Lee, F.C., Qiu, Y., et al., 2008. A novel high-power-density three-level LCC resonant converter with constant-power-factor-control for charging applications. *IEEE Trans. Power Electron.*, **23**(5):2411-2420. [doi:10.1109/TPEL.2008.2002052]
- Gibalov, V.I., Pietsch, G.J., 2000. The development of dielectric barrier discharges in gas gaps and on surfaces. *J. Phys. D Appl. Phys.*, **33**(20):2618-2636. [doi:10.1088/0022-3727/33/20/315]
- Gilbert, A.J., Bingham, C.M., Stone, D.A., et al., 2007. Normalized analysis and design of LCC resonant converters. *IEEE Trans. Power Electron.*, **22**(6):2386-2402. [doi:10.1109/TPEL.2007.909243]
- Gilbert, A.J., Bingham, C.M., Stone, D.A., et al., 2008. Self-oscillating control methods for the LCC current-output resonant converter. *IEEE Trans. Power Electron.*, **23**(4):1973-1986. [doi:10.1109/TPEL.2008.925198]
- Jidenko, N., Petit, M., Borra, J.P., 2006. Electrical characterization of microdischarges produced by dielectric barrier discharge in dry air at atmospheric pressure. *J. Phys. D Appl. Phys.*, **39**(2):281-293. [doi:10.1088/0022-3727/39/2/008]
- Kinnares, V., Hothongkham, P., 2010. Circuit analysis and modeling of a phase-shifted pulsewidth modulation full-bridge-inverter-fed ozone generator with constant applied electrode voltage. *IEEE Trans. Power Electron.*, **25**(7):1739-1752. [doi:10.1109/TPEL.2010.2042075]
- Kostov, K.G., Nishime, T.M.C., Hein, L.R.O., et al., 2013. Study of polypropylene surface modification by air dielectric barrier discharge operated at two different frequencies. *Surf. Coat. Technol.*, **234**:60-66. [doi:10.1016/j.surfcoat.2012.09.041]
- Liu, Y., He, X., 2005. PDM and PFM hybrid control of a series-resonant inverter for corona surface treatment. *IEE Proc.-Electr. Power Appl.*, **152**(6):1445-1450. [doi:10.1049/ip-epa:20045270]
- Martin-Ramos, J.A., Pernia, A.M., Diaz, J., et al., 2008. Power supply for a high-voltage application. *IEEE Trans. Power Electron.*, **23**(4):1608-1619. [doi:10.1109/TPEL.2008.925153]
- Shafiei, N., Pahlevaninezhad, M., Farzanehfard, H., et al., 2011. Analysis and implementation of a fixed-frequency LCLC resonant converter with capacitive output filter. *IEEE Trans. Ind. Electron.*, **58**(10):4773-4782. [doi:10.1109/TIE.2011.2116758]
- Shafiei, N., Pahlevaninezhad, M., Farzanehfard, H., et al., 2013. Analysis of a fifth-order resonant converter for high-voltage DC power supplies. *IEEE Trans. Power Electron.*, **28**(1):85-100. [doi:10.1109/TPEL.2012.2200301]
- Wagner, H.E., Brandenburg, R., Kozlov, K.V., et al., 2003. The barrier discharge: basic properties and applications to surface treatment. *Vacuum*, **71**(3):417-436. [doi:10.1016/S0042-207X(02)00765-0]
- Wang, C., He, X., 2006. Preparation of hydrophobic coating on glass surface by dielectric barrier discharge using a 16 kHz power supply. *Appl. Surf. Sci.*, **252**(23):8348-8351. [doi:10.1016/j.apsusc.2005.11.042]
- Wang, H., Fang, Z., Qiu, Y., et al., 2005. On the changing of equivalent capacitance in dielectric barrier discharge. *Insul. Mater.*, **38**(1):37-40. [doi:10.3969/j.issn.1009-9239.2005.01.012] (in Chinese).
- Wedaa, H., Abdel-Salam, M., Ahmed, A., et al., 2011. NO removal using dielectric barrier discharges in a multirod reactor stressed by AC and pulsed high voltages. *IEEE Trans. Dielectr. Electr. Insul.*, **18**(5):1743-1751. [doi:10.1109/TDEI.2011.6032846]
- Williamson, J.M., Trump, D.D., Bletzinger, P., et al., 2006. Comparison of high-voltage ac and pulsed operation of a surface dielectric barrier discharge. *J. Phys. D Appl. Phys.*, **39**(20):4400-4406. [doi:10.1088/0022-3727/39/20/016]
- Youssef, M.Z., Jain, P.K., 2007. Series-parallel resonant converter in self-sustained oscillation mode with the high-frequency transformer-leakage-inductance effect: analysis, modeling, and design. *IEEE Trans. Ind. Electron.*, **54**(3):1329-1341. [doi:10.1109/TIE.2007.892742]